

# Signatures of Interstellar-Intracluster Medium Interactions: Spiral Galaxy Rotation Curves in Abell 2029

DANIEL A. DALE

IPAC, California Institute of Technology 100-22, Pasadena, CA 91125

JUAN M. USON

National Radio Astronomy Observatory, 520 Edgemont Road, Charlottesville, VA 22903

## ABSTRACT

We investigate the rich cluster Abell 2029 ( $z \sim 0.08$ ) using optical imaging and long-slit spectral observations of 52 disk galaxies distributed throughout the cluster field. No strong emission-line galaxies are present within  $\sim 400$  kpc of the cluster center, a region largely dominated by the similarly-shaped X-ray and low surface brightness optical envelopes centered on the giant cD galaxy. However, two-thirds of the galaxies observed outside the cluster core exhibit line emission.  $H\alpha$  rotation curves of 14 cluster members are used in conjunction with a deep  $I$  band image to study the environmental dependence of the Tully-Fisher relation. The Tully-Fisher zero-point of Abell 2029 matches that of clusters at lower redshifts, although we do observe a relatively larger scatter about the Tully-Fisher relation. We do not observe any systematic variation in the data with projected distance to the cluster center: we see no environmental dependence of Tully-Fisher residuals,  $R - I$  color,  $H\alpha$  equivalent width, and the shape and extent of the rotation curves.

*Subject headings:* galaxies: clusters: individual (Abell 2029) — galaxies: evolution — galaxies: intergalactic medium

## 1. INTRODUCTION

The evolution of galaxies in clusters is affected by ram-pressure stripping, tidal interactions, mergers, accretion, and cooling flows. These processes are expected to be particularly effective in the richest clusters where they are likely to erase any memory

of their initial conditions (Dressler 1984). A rich cluster typically has a conspicuous intracluster medium and a regular, elliptical-dominated core (Sarazin 1986). The spiral galaxies of a rich cluster are predominantly distributed in the periphery of the cluster, and the closer a spiral disk is to the cluster center, the less likely it is to contain neutral hydrogen gas (Giovanelli & Haynes 1985). Moreover, the frequency and strength of optical emission lines are lower in cluster galaxies, as first suggested by Osterbrock (1960) and later verified with large samples of field and cluster galaxies (Gisler 1978; Dressler et al. 1985; Balogh et al. 1999). This trend has been shown to correlate with cluster-centric distance, and is not solely due to morphological segregation (Balogh et al. 1997). This lack of interstellar gas within cluster galaxies may be due to evaporation into the hotter intracluster gas, or it may be attributed to stripping originating from either tidal galaxy-galaxy interactions or ram pressure ablation on intracluster gas. Ram pressure ablation, which involves the loss of interstellar gas due to rapid motion through intracluster gas, was first pointed out by Gunn and Gott (1972) as the likely cause of mass loss of spiral galaxies in clusters, and optical and 21 cm observations give direct evidence of this process (Haynes 1990; Kenney & Koopman 1999). In fact, spiral galaxies that pass through the centers of rich clusters are likely to lose up to 90% of their interstellar H I (Roberts & Haynes 1994). For example, H I observations of the Virgo cluster and of Abell 2670 (located at a redshift of  $z \sim 0.08$  and considerably richer than Virgo) show them to be quite different. Indeed, the “stripping radius” (the distance from the cluster center inside which spiral galaxies are H I deficient) is two to three times larger in Abell 2670 than in the Virgo cluster (van Gorkom 1996).

Such dramatic environmental effects could affect a variety of observations. Whitmore, Forbes, & Rubin (1988) showed that spiral galaxies within clusters exhibit falling rotation curves, as opposed to the asymptotically flat or rising rotation curves usually seen in galaxies located in the periphery of clusters as well as in the field; Adami et al. (1999) show similar results for late-type spiral galaxies. Furthermore, they find that rotation curves of cluster galaxies may be of lower amplitude than those of field galaxies. They offer the explanation that the falling (and lower amplitude) rotation curves are due to mass loss—the inner galaxies have had their dark matter halos stripped—or that the cluster environment simply inhibits halo formation. They also find a monotonic increase in the mass to light ratio with distance to the cluster center which they ascribe to the changing shape of the rotation curves with cluster position. This view has been contested, however, by Amram et al. (1993) and Vogt (1995) who find little evidence for any gradients in the outer portions of rotation curves. Clusters, the peaks of the density hierarchy, have undergone strong merger activity, both in terms of large-scale subclumps (Girardi et al. 1997) and at the galaxy level, as in the formation of cDs. In short, there is a large body of work that suggests that the spiral galaxy population in dense clusters is fundamentally different to spiral systems

found in regions of lower density.

Abell 2029 is one of the densest and richest clusters in the Abell catalog of rich clusters of galaxies and thus provides an important laboratory in which to study the effects of the intracluster medium. It is located at a distance of  $\sim 240h^{-1}$  Mpc (we write the Hubble constant in the form  $100h$  km s $^{-1}$  Mpc $^{-1}$ ), and extensive redshift studies have determined its velocity dispersion to be  $\sim 1500$  km s $^{-1}$  (Dressler 1981; Bower, Ellis, & Efstathiou 1988). In addition, it has been (re)classified as an Abell richness class 4.4 cluster (Dressler 1978). The cluster is a textbook example of a compact, relaxed, cD galaxy-dominated cluster with a high intracluster X-ray luminosity ( $1.1 \times 10^{45}h^{-2}$  ergs s $^{-1}$ ; David et al. 1993). The cD galaxy is one of the largest galaxies known, with low surface brightness emission detected out to a radius of  $0.6h^{-1}$  Mpc (Uson, Boughn, & Kuhn 1991).

We have obtained a large set of rotation curves of galaxies located in the field of Abell 2029 in order to study the environmental effects due to the cluster by comparing our data to the *I* band Tully-Fisher template relation for clusters obtained by Giovanelli et al. (1997) and Dale et al. (1999; hereafter G97 and D99 respectively). This relation was derived from the application of the Tully-Fisher relation to more than 1000 galaxies located in 76 clusters, of which 75 are Abell richness class 2 or lower. Our observations are described in Section 2 and the results are presented in Section 3. The implications of this work are discussed in Section 4.

## 2. The Data

### 2.1. Optical Spectroscopy

We obtained long-slit spectroscopy to derive optical rotation curves of galaxies in Abell 2029. The observations were carried out at the Mt. Palomar 5 m telescope during the nights of 1998 April 27–29. We used the red camera of the Double Spectrograph (Oke and Gunn 1982) to observe the H $\alpha$  (6563 Å), [N II] (6548, 6584 Å), and [S II] (6717, 6731 Å) emission lines. The spatial scale of CCD21 (1024 $^2$ ) was 0".468 pixel $^{-1}$ . The combination of the 1200 lines mm $^{-1}$  grating and a 2" wide slit yielded a dispersion of 0.65 Å pixel $^{-1}$  and a spectral resolution of 1.7 Å (equivalent to 75 km s $^{-1}$  at 6800 Å). The grating angle allowed us to observe H $\alpha$  in galaxies with recessional velocities between 7,600 and 38,100 km s $^{-1}$ .

We were fortunate to enjoy extremely mild atmospheric conditions at Mt. Palomar. All three nights were photometric and dark. The seeing was remarkably sharper and more stable than typically encountered at the site; we estimate the median seeing to have been 1", but at times the seeing dropped to 0".6. Such excellent spatial resolution is important

to obtain high sensitivity rotation curves at the redshifts of the target galaxies. Besides yielding higher signal-to-noise per pixel, a sharper seeing also allows a more accurate placement of the slit. This is important because slit offsets and incorrect estimations of the position angles of galaxy disks can lead to serious errors in the inferred velocity widths (Bershady 1998, Giovanelli et al. 2000; hereafter G00). We did not obtain absolute flux calibrations as they were not necessary for the purpose of this paper.

We used deep  $R$  and  $I$  band images to select candidate galaxies as well as to estimate their position angles. We discuss these data in the next section. We observed all probable disk-like systems on the reference images that might be members of the cluster, did not appear to be face-on, and were free of contamination from foreground stars. The limited resolution of the reference images precluded unambiguous identification of appropriate Tully-Fisher candidates. Our observing strategy began with a five minute test-exposure on each spectroscopic target. That way we were able to estimate “on the fly” the exposure time required in order to sample adequately the outer disk regions. Furthermore, the test exposure determined whether the galaxy was even useful to our work; a galaxy may lie in the foreground or background of the cluster or it may contain little or no  $H\alpha$  emission. If the observation was deemed useful, a second exposure typically ranged between 15 and 45 minutes. We detected line emission in half of the 52 observed galaxies. We list the galaxies observed in Table 1, sorting the entries by Right Ascension. The table contains:

Col. 1: Identification names corresponding to a coding number in our database, referred to as the Arecibo General Catalog.

Cols. 2 and 3: Right Ascension and Declination in the 1950.0 epoch. Coordinates have been obtained from the Digitized Sky Survey catalog and are accurate to  $< 2''$ .

Col. 4: The galaxy radial velocity as measured in the heliocentric reference frame. The redshift measurements of the galaxies without emission lines were obtained from the NED<sup>1</sup> database. They have been previously derived by others using absorption-line spectra.

Col. 5: An indication of the usefulness of the optical emission lines in order to apply the Tully-Fisher relation: 0=no lines present; 1=strong emission lines throughout much of the disk; 2=weak or nuclear emission only.

Rotation curves are extracted as discussed in Dale et al. (1997 and 1998; hereafter D97 and D98). We use the  $H\alpha$  emission line to map the rotation curve except in the case of the galaxy AGC 251909 where the emission of the  $[N II]$  line ( $6584 \text{ \AA}$ ) extends to a larger

---

<sup>1</sup>The NASA/IPAC Extragalactic Database is operated by the Jet Propulsion Laboratory, California Institute of Technology, under contract with the National Aeronautics and Space Administration.

distance than that of the  $H\alpha$  emission. We center the rotation curve kinematically by assigning the velocity nearest to the average of the 10% and 90% velocities to be at radius zero, where an N% velocity is greater than N% of the velocity data points in the rotation curve. The average of the 10% and 90% velocities is taken to be the galaxy’s recessional velocity. We define the observed rotational velocity width to be  $W_{\text{obs}} \equiv V_{90\%} - V_{10\%}$ . We filled-in small portions of the  $H\alpha$  rotation curve of two galaxies (AGC 251913 and AGC 251912) using data from the [N II] rotation curve in order to provide information on the shape of the inner parts and to ensure consistent estimates of  $W_{\text{obs}}$ .

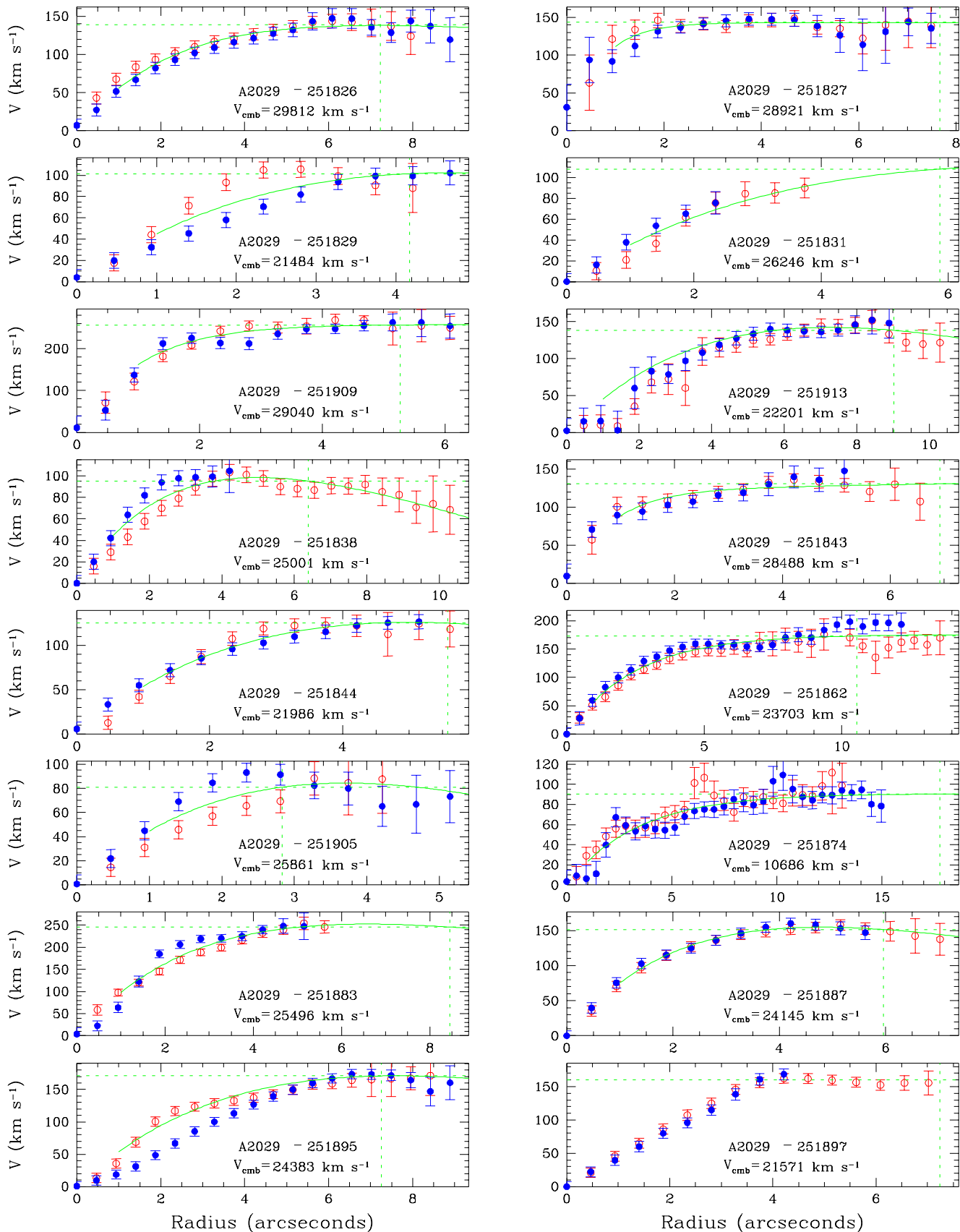
The rotation curves in our sample vary in physical extent, and more importantly, they do not all reach the optical radius,  $R_{\text{opt}}$ , the distance along the major axis to the isophote containing 83% of the  $I$  band flux. This radius is reported by Persic & Salucci (1991) and G00 to be the most useful radius at which to measure the velocity width of rotation curves. We have extrapolated the rotation curves, and hence made adjustments to  $W_{\text{obs}}$ , when they did not reach  $R_{\text{opt}}$ . The resulting correction,  $\Delta_{\text{sh}}$ , depends on the shape of the rotation curve and only exceeded 4% for AGC 251831 where the correction was large ( $\sim 44\%$ ).

To recover the actual velocity widths, a few more corrections are necessary. The first is the factor  $1/\sin i$  to convert the width observed when a disk is inclined to the line of sight at an angle  $i$  to what would be observed if the disk were edge-on, and the second is the factor  $1/(1+z)$  to correct the cosmological broadening of  $W$ . A final correction,  $f_{\text{slit}} < 1.05$ , accounts for the finite width of the slit of the spectrograph (G00). The corrected optical rotational velocity width is

$$W_{\text{cor}} = \frac{W_{\text{obs}} + \Delta_{\text{sh}}}{(1+z) \sin i} f_{\text{slit}}. \quad (1)$$

A discussion of the errors in the velocity widths can be found in D97.

Figure 1 is a display of the rotation curves observed in the field of Abell 2029. Entries in the figure are sorted by Right Ascension. The name of the galaxy is given along with the CMB radial velocity. Two dashed lines are drawn: the vertical line is at  $R_{\text{opt}}$ ; the horizontal line indicates the adopted half-velocity width,  $W/2$ , which in some cases arises from an extrapolation to the rotation curve (see Table 1). Overlaid are the fits used to infer  $W(R_{\text{opt}})$ . Details of the fitting procedure can be found in G00. The error bars include both the uncertainty in the wavelength calibration and the routine used to fit the rotation curve. Notice that the data are highly correlated due to seeing and guiding jitter. This is properly taken into account by the fitting routines (see D97 and references therein for details).



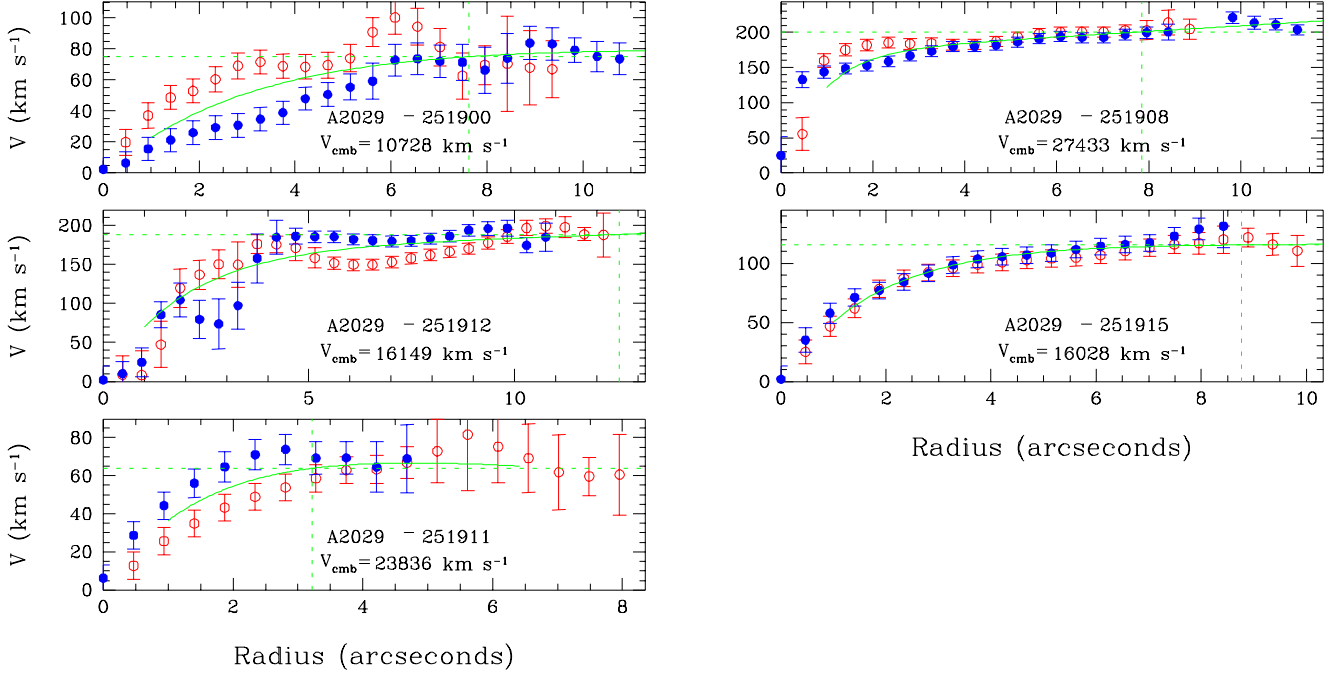


Fig. 1.— The kinematically folded rotation curves (see text). The error bars include both the uncertainty in the wavelength calibration and the rotation curve fitting routine used. Names of the galaxy are given along with the CMB radial velocities. Two dashed lines are drawn: the horizontal line indicates the adopted half velocity width,  $W/2$ , which in some cases arises from an extrapolation to the RC; the vertical line is at  $R_{\text{opt}}$ , the radius containing 83% of the  $I$  band flux. A fit to the rotation curve is indicated by a solid line. Note that the rotation curves are *not* deprojected to an edge-on orientation.

We list in Table 2 the complete set of spectroscopic data corresponding to the 21 galaxies for which we obtained useful rotation curves, sorting the entries by Right Ascension. The parameters listed in Table 2 are:

Col. 1: Identification names corresponding to a coding number in the Arecibo General Catalog.

Col. 2: The spectral exposure time in seconds.

Col. 3: The recessional velocity of the galaxy in the CMB reference frame, assuming a Sun-CMB relative velocity of  $369.5 \text{ km s}^{-1}$  towards  $(l, b) = (264.4^\circ, 48.4^\circ)$  (Kogut et al. 1993). Errors are parenthesized: e.g.  $13241(08)$  means  $13241 \pm 08$ .

Col. 4: The observed velocity width in  $\text{km s}^{-1}$ .

Col. 5: The velocity width in  $\text{km s}^{-1}$  at  $R_{\text{opt}}$  after correcting for the shape of the rotation curve, the cosmological broadening, and the smearing effects due to the finite width of the slit of the spectrograph.

Col. 6: The corrected velocity width in  $\text{km s}^{-1}$  converted to an edge-on perspective.

Col. 7: The adopted inclination of the plane of the disk to the line of sight,  $i$ , expressed in degrees, ( $90^\circ$  corresponds to an edge-on perspective); the derivation of  $i$  and its associated uncertainty are discussed in Section 4 of D97.

Col. 8: The logarithm in base 10 of the corrected velocity width (value in column 6), together with its estimated uncertainty in parentheses. The uncertainty takes into account both measurement errors and uncertainties arising from the corrections. The format 2.576(22), for example, is equivalent to  $2.576 \pm 0.022$ .

## 2.2. Optical Imaging

*I* band photometry of Abell 2029 was obtained for a different project by one of us (JMU) in collaboration with S. P. Boughn (Haverford) with the 0.9 m telescope on Kitt Peak National Observatory on 1998 April 19. They used the T2KA camera mounted at the f:7.5 Cassegrain focus which resulted in square pixels,  $0''.68$  on a side. The seeing was excellent, between  $0''.7$  and  $0''.9$ , which resulted in an effective seeing of  $\sim 1''.2$  due to the available pixel size.

Two sets of fifteen partially overlapping frames were used to form a mosaic of about  $35'$  (RA) by  $58'$  (Dec). The central three by three mosaic has overlaps of about  $3/4$  of a frame between immediately adjacent frames, whereas the outer three frames to the north and south overlap by about  $1/2$  of a frame with the closest of the central ones. All but four of the outlying frames to the north and south were obtained with air masses between 1.11 and 1.25. The exposures lasted five minutes. The data were processed as discussed in Uson, Boughn and Kuhn (1991, hereafter UBK91). All frames were used to generate a “sky-flat” gain calibration frame. Since the cluster contains a diffuse halo that surrounds the central galaxy, a  $12'$  by  $12'$  area centered on the cluster was blanked on all the relevant frames before using them to generate the sky flat as discussed in UBK91. The calibrated frames were used to determine the secant-law extinction which had a slope of  $0.06 \text{ mag/airmass}$ .

Absolute calibration was done using stars from Landolt’s *UBVRI* secondary calibration list (Landolt 1983). Details will be given elsewhere.



The  $R$  band photometry was obtained from UBK91.

Flux estimation follows from the data reduction methods discussed in D97 and D98 using both standard and customized IRAF<sup>2</sup> packages. We will only mention here that the measured fluxes, denoted  $m_{\text{obs}}$ , include extrapolations of the exponential fits to the surface brightness profiles to eight disk scale lengths and are typically accurate to  $\sim 0.03$  mag (uncertainties at least as large are later included after making corrections for internal extinction). We apply some corrections to  $m_{\text{obs}}$  in order to obtain the final  $I$  band fluxes:

$$m_I = m_{\text{obs}} - A_I + k_I - \Delta m_{\text{int}}. \quad (2)$$

For the Galactic extinction correction  $A_I$ , we use the recent work of Schlegel, Finkbeiner, and Davis (1998) who have provided accurate Galactic reddening estimates using COBE/DIRBE and IRAS/ISSA dust maps. The internal extinction correction,  $\Delta m_{\text{int}}$ , is applied using the procedure outlined in G97,

$$\Delta m_{\text{int}} = -f(T) \gamma(W_{\text{cor}}) \log(1 - e), \quad (3)$$

where  $\gamma$  ( $\lesssim 1.0$ ) depends on the corrected velocity width  $W_{\text{cor}}$  and  $e$  is the ellipticity of the spiral disk, corrected for atmospheric seeing effects as described in Section 5 of D97 (the adopted correction  $\Delta m_{\text{int}}$  is slightly smaller for early, less dusty galaxies:  $f(T)=0.85$  for types  $T$  earlier than Sbc;  $f(T)=1$  otherwise). We apply a cosmological k-correction according to Han (1992):  $k_I = (0.5876 - 0.1658T)z$ .

The relevant photometric data are listed in Table 3 with the first column matching that of Table 2. The remaining parameters are:

Col. 2: Morphological type code in the RC3 scheme, where code 1 corresponds to Sa's, code 3 to Sb's, code 5 to Sc's and so on. We assign these codes after visually inspecting the CCD  $I$  band images and after noting the value of  $R_{75}/R_{25}$ , where  $R_X$  is the radius containing X% of the  $I$  band flux. This ratio is a measure of the central concentration of the flux which was computed for a variety of bulge-to-disk ratios. Given the limited resolution of the images, some of the inferred types are rather uncertain; uncertain types are followed by a colon.

Col. 3: The angular distance  $\theta$  in arcminutes from the center of each cluster.

Col. 4: Position angle used for spectrograph slit positioning (North:  $0^\circ$ , East:  $90^\circ$ ).

Col. 5: Ellipticity of the disk corrected for seeing effects as described in Sec. 5 of D97, along with its corresponding uncertainty expressed using the same convention as in Table 2.

---

<sup>2</sup>IRAF (Image Reduction and Analysis Facility) is distributed by NOAO.

Col. 6: The (exponential) disk scale length in arcseconds.

Col. 7: The distance along the major axis to the isophote containing 83% of the  $I$  band flux.

Col. 8: The measured  $I$  band magnitude, extrapolated to 8 disk scale lengths assuming that the surface brightness profile of the disk is well described by an exponential function.

Col. 9: The absolute magnitude, computed assuming that the galaxy is at the distance indicated by the cluster redshift, or by assuming the galaxy is at the distance indicated by the redshift if the galaxy is not deemed to be a member of the cluster. The calculation assumes  $H_o = 100h \text{ km s}^{-1} \text{ Mpc}^{-1}$ , so the value listed is strictly  $M_I - 5 \log h$ . This parameter is calculated after expressing the redshift in the CMB frame and neglecting any peculiar motion. The uncertainty on the magnitude, parenthetically included in hundredths of a mag, is the sum in quadrature of the measurement errors and the estimate of the uncertainty in the corrections applied to the measured parameter.

Col. 10: The difference in the  $R$  and  $I$  band magnitudes.

When an asterisk appears at the end of the line, we include a detailed comment on that particular object. Because of the extent of these comments we have not appended them to the table but have included them in the text. Note that a record is flagged in both Tables 2 and 3, whether the comments refer to the photometry, to the spectroscopy, or to both.

251826: Background galaxy.

251827: Background galaxy; uncertain PA.

251831: Rising rotation curve; large rotation curve extrapolation.

251909: Background galaxy; [N II] rotation curve used.

251913: [N II] patch for radii  $< 3''$ ; uncertain disk ellipticity.

251838: Asymmetric  $I$  band profile.

251843: Note low  $i$ .

251874: Foreground galaxy; 5 minute integration.

251895: Uncertain disk ellipticity; asymmetric  $I$  band profile.

251897: Center-of-light used for rotation curve spatial and kinematic center.

251900: Foreground galaxy; 5 minute integration; center-of-light used to determine the center of the rotation curve.

251908: Tidally interacting with small companion  $13''$  to NE (§3.4).

251912: Foreground galaxy; [N II] patch for radii  $< 3''$ ; flux disentanglement with AGC 251911 difficult.

251911: Flux disentanglement with AGC 251912 difficult; uncertain PA and disk ellipticity.

251915: Foreground galaxy.

### 3. Results

#### 3.1. The Distribution of Emission-Line Galaxies

A plot of the sky distribution of Abell 2029 field objects is displayed in the left panel of Figure 2. Filled (open) circles represent galaxies with fair to strong (weak but detectable)

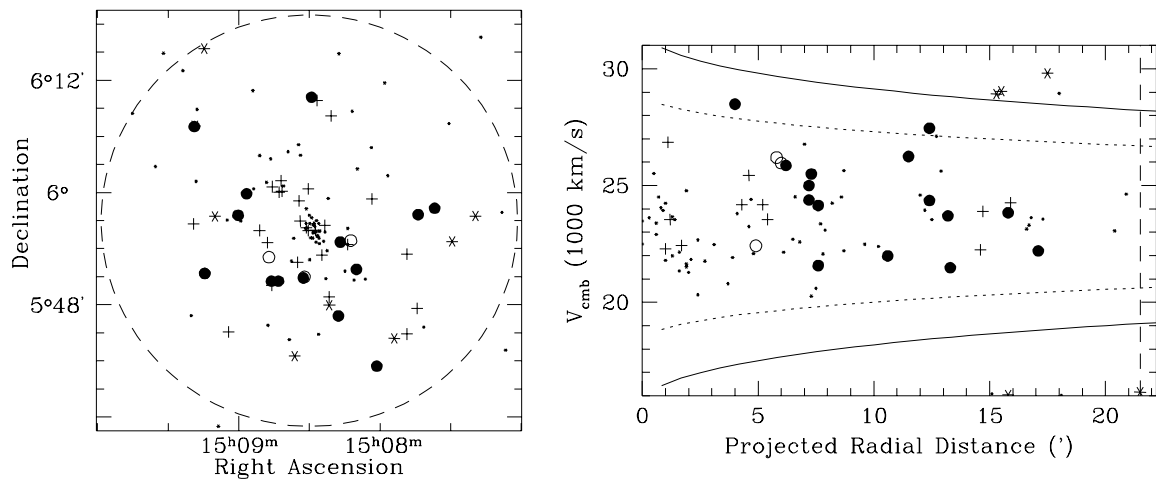


Fig. 2.— Sky and velocity distribution of galaxies in the cluster field. Circles represent cluster members with measured photometry and widths; if unfilled, widths are poorly determined. Asterisks identify foreground and background galaxies, and dots give the location of galaxies with known redshift. Crosses indicate the positions of galaxies lacking emission lines. The dashed line in each panel indicates 1 Abell radius. The dotted and solid lines respectively indicate 2 and  $3\sigma$  cluster membership contours (Carlberg et al. 1997).

optical emission lines. Asterisks mark foreground and background galaxies with observed rotation curves and crosses indicate the positions of observed galaxies lacking emission lines. Other galaxies with known redshifts are indicated by small dots. The right panel in Figure 2 presents galaxy redshifts versus their projected distances from the cluster center. In both panels one Abell radius ( $1.48h^{-1}$  Mpc) is indicated by the dashed line. The redshift measurements of the galaxies lacking emission lines (indicated by crosses) are drawn from the literature.

All the galaxies we observed spectroscopically are projected to lie within one Abell radius, but of course the ultimate definition of cluster membership relies on the observed

redshift distribution. Using spectra for 47 cluster galaxies, Dressler (1981) found a velocity dispersion of  $1430 \text{ km s}^{-1}$  for the cluster. This was confirmed by Bower et al. (1988) for both the inner and outer regions of the cluster using a similar sample size. Combining our observations with those reported in the literature yields a redshift sample twice as large ( $N = 99$ ) as those used previously. We find a mean CMB cluster velocity of  $23,657 \pm_{99}^{216} \text{ km s}^{-1}$  and a  $1\sigma$  (rest frame) velocity dispersion of  $1454 \text{ km s}^{-1}$ . The cluster systemic velocity agrees well with the CMB redshift velocity of the cD galaxy:  $23,550 \text{ km s}^{-1}$  (de Vaucouleurs et al. 1991). This is not surprising given that the cD galaxy is about 100 times more luminous than any other cluster member (UBK91). We derive (projected) cluster membership contours using the results from the CNOC survey of galaxy clusters (Carlberg et al. 1997), scaled by our estimate of the cluster velocity dispersion for Abell 2029. The  $3\sigma$  contour is indicated by the two solid curves in the right-hand panel and, coupled with the Abell radius of 21.5, represents our working definition of the cluster proper; the dotted curves show the  $2\sigma$  contour (see, for example, Balogh et al. 1999).

The most striking aspect of Figure 2 is the paucity of observed emission line galaxies located in the cluster core. We observed 17 of the galaxies that are projected to lie within the inner  $5'$  ( $\sim 340h^{-1} \text{ kpc}$ ) of the cluster, and the only one exhibiting a strong emission line is outside the  $2\sigma$  cluster-membership contour. Of the remaining 16 inner-cluster galaxies observed, one has a weak  $H\alpha$  line, but the other 15 galaxies show no emission lines at all in a 300 second test observation. Our success rate was much higher when observing galaxies that are projected to lie further than  $5'$  from the cluster center. Indeed, 24 of the 35 galaxies observed in that area had emission lines that were detected in the 5 minute test exposure.

An alternative display of such data is presented in Figure 3. Here we show the relative spatial distribution of the galaxies exhibiting strong, weak, and no  $H\alpha$  emission after accounting for the non-circular orientation of the projected diffuse optical light of the cD galaxy. The counts are computed in elliptical bins of constant axis ratio 2:1, centered on the cD and oriented at a position angle  $21^\circ$  East of North (UBK91); the X-ray brightness contours are consistent with this morphology (Slezak, Durret & Gerbal 1994). Again, there is a fairly clear delineation between regions with many  $H\alpha$ -rich galaxies and regions without  $H\alpha$ -emitting galaxies. For comparison purposes we note that UBK91 found that approximately 90% of the projected  $R$  band emission of the cD galaxy falls within an ellipse with a semi-minor axis of about  $4'$ .

### 3.2. Tully-Fisher Data

The Tully-Fisher data for all members of Abell 2029 are presented in Figure 4. Included

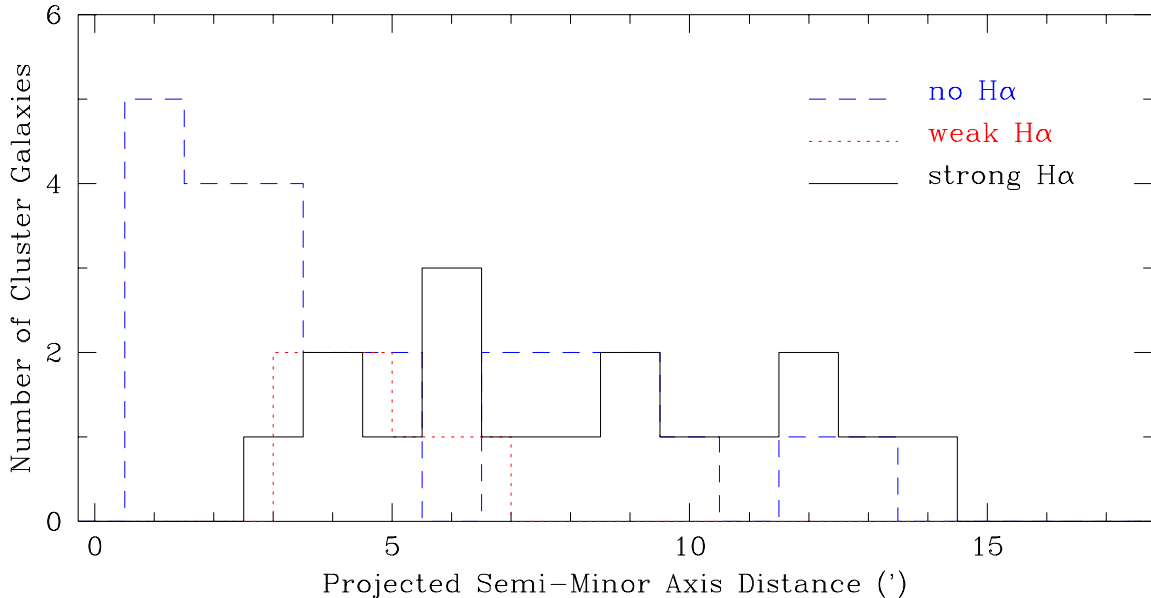


Fig. 3.— The spatial distribution of observed cluster galaxies as a function of the projected distance from the cD galaxy’s semi-minor axis, separated according to the strength of the observed H $\alpha$  line emission. The counts are computed from within elliptical bins of constant axis ratio 2:1 and oriented at a position angle 21° East of North.

in the Tully-Fisher plot is the template relation obtained from the cluster Tully-Fisher study of D99:

$$y = -7.68x - 20.91 \quad (4)$$

where  $y$  is  $M_I - 5 \log h$  and  $x$  is  $\log W_{\text{cor}} - 2.5$ . The data are corrected for the effects described in Section 2. In addition, the morphological type offsets for early-type disk galaxies advocated by G97 and D97 are applied to three galaxies:  $\Delta m_T = -0.1$  mag for the Sb galaxy AGC 251913, and  $\Delta m_T = -0.32$  mag for AGC 251862 (Sa) and AGC 251912 (S0/a). The scatter in the Tully-Fisher data is 0.56 mag, considerably larger than the values of 0.35 and 0.38 mag found in G97 and D99, respectively. Notice the absence of a detectable offset between the Abell 2029 data and the Tully-Fisher template. Although we have not included any corrections for Malmquist bias, typically of order 0.04 magnitudes for clusters with 10 or more Tully-Fisher measurements (D99), it gives us great confidence in our data reduction procedures as the  $I$  band photometry was reduced independently of this project.

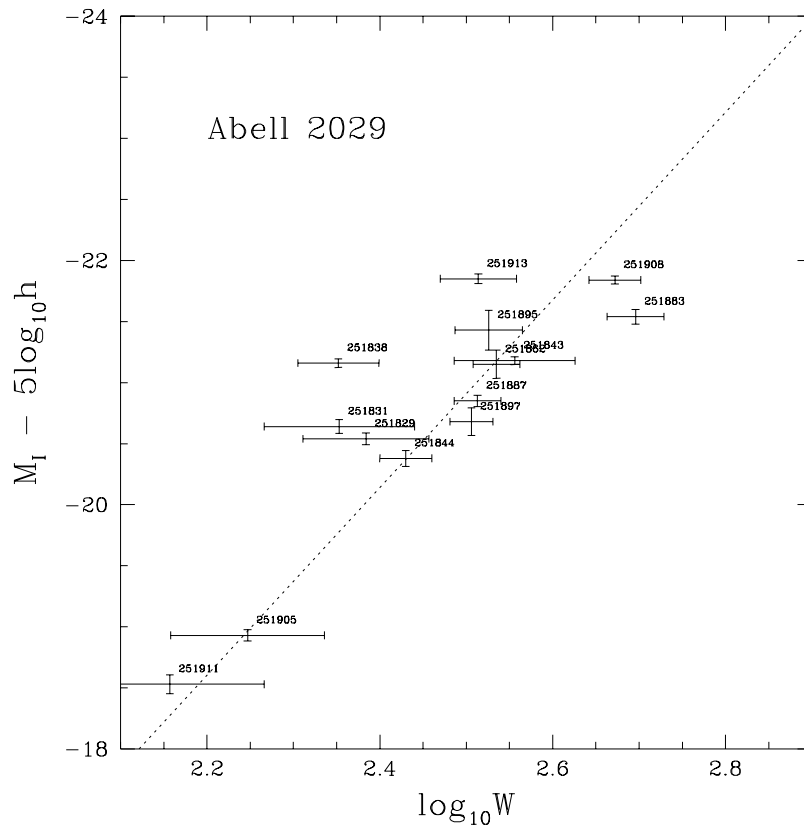


Fig. 4.— The Tully-Fisher data for Abell 2029, uncorrected for cluster peculiar motion. The dashed line is the template relation for clusters obtained by D99, Eqn. 4.

### 3.3. Are There Other Trends with Cluster Environment?

Plotted in Figure 5 are some properties of the emission-line galaxies as a function of projected distance from the cluster center. Filled (open) circles represent cluster (foreground and background) galaxies. The top panel displays the residuals of the Tully-Fisher data. An overly large  $M/L$  ratio would correspond to an overly fast rotating disk for a given absolute magnitude, i.e. the galaxy would appear fainter than the fiducial template would indicate and hence would have a positive residual. An increasing  $M/L$  ratio with increasing projected distance, as advocated by Whitmore, Forbes & Rubin (1988) and Adami et al. (1999), would thus appear as a trend of increasing residuals with increasing projected distance. Such a trend is not present in the data. In fact, the slight trend seen for cluster galaxies acts in the opposite sense.

The data in Panels b and c show that no trend in  $R - I$  color or in the physical extent of the rotation curve with distance between the galaxy and the center of the cluster ( $R_{\max}$  is the maximum radial distance at which the rotation curve is measured). The shape of the rotation curve (Panel d), and the  $H\alpha$  equivalent width (Panel e) seem uncorrelated as well with location in the cluster. The “shape” of a rotation curve is defined here as the outer gradient of the rotation curve, namely

$$\text{Rotation Curve Shape} = \frac{W(R_{\text{opt}}) - W(0.5R_{\text{opt}})}{W(R_{\text{opt}})}. \quad (5)$$

### 3.4. A Tidal $H\alpha$ Bridge Between AGC 251908 and its Companion

One reason why we took spectra of all plausible disk systems in the cluster core was to try to observe the tidal stripping of a galaxy passing through a dense intracluster medium. For example, AGC 250201 is a possible candidate as it lies well within the low surface brightness envelope of the cD galaxy but has a redshift more than  $3000 \text{ km s}^{-1}$  higher than the cD. Unfortunately, no core galaxies show strong emission lines as discussed above. We did observe, however, a bridge of  $H\alpha$  emission connecting one pair of galaxies outside the cluster core: AGC 251908 and its small satellite/companion galaxy located approximately  $13''$  to the NW. The joint rotation curve for this pair is displayed in Figure 6. The companion is amorphous in  $I$  band and has a FWHM of  $1''.7$ . The flux in a circular aperture of radius  $2''.7$  centered on the companion corresponds to a magnitude of  $m_I = 19.87$ , or  $M_I = -17.08$ . No such bridge is evident in the  $I$  band image, nor is any obvious warping seen in the disk of AGC 251908.

This region of the sky was unfortunately not covered by our  $R$  band map, so we turn to the Palomar Observatory Sky Survey II<sup>3</sup> data ( $1''$  pixels) for further clues. We notice that the companion has a different morphology on the POSS-II red plate, the plate whose filter bandpass includes the  $H\alpha$  line. The emission from the companion is significantly more extended ( $3''.4$  FWHM) at this wavelength, and it clearly has an elongated shape. It is reasonable to assume that the companion is a disk galaxy since we see  $H\alpha$  in emission. Moreover, we estimate the position angle of the major axis of the disk to be  $45^\circ$ , essentially perpendicular to the angle used for the long-slit observation of AGC 251908. Thus it is not surprising that we detected little rotation of the companion galaxy.

---

<sup>3</sup>The Second Palomar Observatory Sky Survey was made by the California Institute of Technology with funds from the National Science Foundation, the National Geographic Society, the Sloan Foundation, the Samuel Oschin Foundation, and the Eastman Kodak Corporation.

#### 4. Discussion

The extended optical envelope centered on the cD galaxy in Abell 2029 was interpreted by UBK91 as the leftover of a period of violent relaxation during the initial cluster collapse. This process would have led as well to the ionization of the gas present in the galaxies that participated in such a collapse and to the hot intracluster gas, observable through its X-ray emission and strongly peaked at the cluster center. The galaxies that traverse the cluster core will have their interstellar gas stripped by the dense intracluster gas, and is likely the root cause of the lack of emission line signatures from these galaxies. Indeed, UBK91 show the extremely large extent of the  $R$  band profile which they trace to  $\sim 5'$ , a boundary similar to the delineation between emission-poor and relatively emission-rich environs. Beyond this distance, however, it appears that the projected distance from the cluster core at which a cluster galaxy lies plays only a small role in the  $H\alpha$  success rate: galaxies with emission lines are spatially evenly mixed with those galaxies lacking emission lines.

A goal of this project was to search for signs of tidal stripping on inner-core galaxies. Therefore, we observed all disk systems in the cluster core, irrespective of whether or not the galaxy appeared to be a useful “Tully-Fisher” galaxy. This could mean that we inspected a large fraction of early type spirals (S0 to Sab) in the cluster core. In the Coma cluster, for example, S0 galaxies outnumber spirals in the cluster center by more than a factor of two (Andreon & Davoust 1997). We find that the average (RC3) morphological type for the emission line galaxies that we observed in Abell 2029 is  $T = 4.7$  (Sbc/Sc), whereas it is  $T = 3.2$  (Sb/Sbc) for the non-emission line galaxies. There is a small difference in the average morphological type of these two groups, and thus the discrepancy in the spatial distribution of emission line galaxies may not be quite so surprising, as early-type disk galaxies contain fewer H II regions than are typically found in late-type spirals.

Outside the cluster core, we find no trends in  $R - I$  color,  $H\alpha$  equivalent width, the shape and physical extent of a rotation curve, nor Tully-Fisher characteristics as a function of projected distance from the cluster center. The latter result is in agreement with the Tully-Fisher work of Biviano et al. (1990) and G97 at relatively low redshifts, as well as with the work at  $0.2 < z < 0.6$  described in D99.

The dispersion in the Tully-Fisher plot for Abell 2029 is about 50% larger than what is seen in clusters at lower redshifts (0.56 mag vs. 0.35 – 0.38 mag). The dispersion does not significantly change if each galaxy is placed at the distance indicated by its individual redshift, rather than assuming that all cluster galaxies are at the same distance. Because of the relative difficulty in assessing such galactic properties as disk inclination and major axis position angle, such an increase is not surprising given the larger measurement uncertainties. However, it is also possible that the strong intracluster medium environment of Abell 2029



promotes a wider variety of  $M/L$  ratios than what is typically found in other clusters. In other words, rich clusters of galaxies may have a higher intrinsic contribution to the overall Tully-Fisher scatter. Using their sample of 522 late-type galaxies in 52 lower redshift Abell clusters, D99 find an intrinsic scatter of 0.25 magnitudes; measurement uncertainties account for the remaining 0.28 magnitudes of the overall scatter. Similar numbers have been found for the Tully-Fisher samples of G97 and Willick (1999). In Abell 2029, we find that measurement uncertainties are responsible for 0.40 magnitudes of the scatter, and thus we infer an intrinsic scatter of 0.39 magnitudes. In short, the relatively large Tully-Fisher dispersion for Abell 2029 appears to be a consequence of both increased measurement uncertainties and relatively larger variations in the spiral galaxy population.

Finally, the overall offset of the Abell 2029 Tully-Fisher data, with respect to the fiducial template relation for lower  $z$  clusters, is indistinguishable from a null offset (at least to within the 0.15 magnitude accuracy of the Abell 2029 zero-point estimation and ignoring the small Malmquist bias correction). If offsets are interpreted as due to peculiar motions, the Abell 2029 offset implies the cluster is essentially at rest in the CMB frame ( $30 \pm 1600$  km s<sup>-1</sup>). Alternatively, this negligible offset may be construed as an indication that little evolution in the Tully-Fisher relation has taken place in clusters up to  $z \sim 0.08$ . However, a much larger sample of clusters at higher redshift is needed to make such a claim statistically significant. In any case, this null result gives us great confidence in the soundness of our data reduction procedures as it results from the combination of spectroscopic and photometric data that were obtained and reduced independently for different projects.

We would like to thank Riccardo Giovanelli and Jacqueline van Gorkom for many helpful comments and Martha Haynes for her assistance in the preparation of the observing run. We thank Steve Boughn for his permission to use the unpublished  $I$  band mosaic observations of Abell 2029. JMU wishes to thank Prof. A. Morales for his hospitality and the “Fundacion BBV” for its financial support of a sabbatical leave at the Laboratorio de Fisica Nuclear of the Universidad de Zaragoza (Spain) during which this paper was completed. The results presented here are based on observations carried out at the Palomar Observatory (PO) and at the Kitt Peak National Observatory (KPNO). KPNO is operated by Association of Universities for Research in Astronomy, Inc., under contract with the National Science Foundation. The Hale telescope at the PO is operated by the California Institute of Technology under a cooperative agreement with Cornell University and the Jet Propulsion Laboratory. The NRAO is a facility of the National Science Foundation which is operated under cooperative agreement by Associated Universities, Inc. This research was supported by NSF grant AST96–17069.

## REFERENCES

- Adami, C., Marcelin, M., Amram, P. & Russeil, D. 1999, *A&A*, 349, 812
- Andreon, S. & Davoust, E. 1997, *A&A*, 319, 747
- Amram, P., Sullivan, W.T., Balkowski, C., Marcelin, M., & Cayatte, V. 1993, *ApJ*, 403, L59
- Balogh, M.L., Morris, S.L., Yee, H.K.C., Carlberg, R.G. & Ellingson, E. 1997, *ApJ*, 488, L75
- Balogh, M.L., Morris, S.L., Yee, H.K.C., Carlberg, R.G. & Ellingson, E. 1999, *ApJ*, 527, 54
- Bershady, M.A., Haynes, M.P., Giovanelli, R. & Andersen, D.R. 1998, in *Galaxy Dynamics*, ed. D. Merritt et. al. (ASP Conference Series); astro-ph/9812020
- Biviano, A., Giuricin, G., Mardirossian, F., & Mezzetti, M. 1990, *ApJS*, 74, 325
- Bower, R.G., Ellis, R.S. & Efstathiou, G. 1988, *MNRAS*, 234, 725
- Carlberg, R.G., Yee, H.K.C., & Ellingson, E. 1997, *ApJ*, 479, 503
- Dale, D.A., Giovanelli, R., Haynes, M.P., Scodreggio, M., Hardy, E. & Campusano, L. 1997, *AJ*, 114, 455 [D97]
- Dale, D.A., Giovanelli, R., Haynes, M.P., Scodreggio, M., Hardy, E. & Campusano, L. 1998, *AJ*, 115, 418 [D98]
- Dale, D.A., Giovanelli, R., Haynes, M.P., Campusano, L. & Hardy, E. 1999, *AJ*, 118, 1468 [D99]
- David, L.P., Slyz, A., Jones, C., Forman, W., Vrtilik, S.D. & Arnaud, K.A. 1993, *ApJ*, 412, 479
- de Vaucouleurs, G., de Vaucouleurs, A., Corwin, H.G., Buta, R.J., Paturel, G. & Fouqué, P. 1991, *Third Reference Catalogue of Bright Galaxies* (New York: Springer)
- Dressler, A. 1978, *ApJ*, 226, 55.
- Dressler, A. 1981, *ApJ*, 243, 26.
- Dressler, A. 1984, *ARA&A*, 22, 185.
- Dressler, A., Thompson, I., & Shectman, S. 1985, *ApJ*, 288, 481

- Giovanelli, R. & Haynes, M.P. 1985, ApJ, 292, 404
- Giovanelli, R., Haynes, M.P., Herter, T., Vogt, N.P., da Costa, L.N., Freudling, W., Salzer, J.J., & Wegner, G. 1997, AJ, 113, 53 [G97]
- Giovanelli, R., Dale, D.A., Haynes, M.P. & Hardy, E. 2000, AJ, submitted [G00]
- Girardi, M., Escalara, E., Fadda, D., Guiricin, G., Mardirossian, F. & Mezzetti, M. 1997, ApJ, 482, 41
- Gisler, G. 1978, MNRAS, 183, 633.
- Gunn, J. & Gott, J. 1972, ApJ, 176, 1
- Han, M. 1992, ApJS, 81, 35
- Haynes, M. P. 1990, in *Clusters of Galaxies*, eds. W.R. Oegerle, M.J. Fitchett & L. Danly (New York: Cambridge University Press), p. 177
- Jorgensen, I., Hjorth, J., Franx, M., & Van Dokkum, P. 1997, BAAS, 190
- Kenney, J.D.P. & Koopman, R.A. 1999, AJ, 117, 181
- Kogut, A. et al. 1993, ApJ, 419, 1
- Landolt, A. U. 1983, AJ, 88, 439
- Oke, J.B. & Gunn, J.E. 1982, PASP, 94, 586
- Osterbrock, D. 1960, ApJ, 132, 325.
- Persic, M. & Salucci, M. 1991, ApJ, 368, 60
- Roberts, M. S. & Haynes, M. P. 1994, ARA&A, 32, 115
- Sarazin, C. 1986, Rev. Mod. Phys., 58, 1
- Schlegel, D.J., Finkbeiner, P.F., & Davis, M. 1998, ApJ, 499, 525
- Slezak, E., Durret, F. & Gerbal, D. 1994, AJ, 108, 1996
- Uson, J. M., Boughn, S. P., and Kuhn, J. R. 1991, ApJ, 369, 46 [UBK91]
- van Gorkom, J. 1996, in *The Minnesota Lectures on Extragalactic Hydrogen*, ed. E.D. Skillman, ASP Conference Series, Vol. 106, p. 293

Vogt, N.P. 1995. Ph.D. thesis, Cornell University

Whitmore, B.C., Forbes, D.A., & Rubin, V.C. 1988, ApJ, 333, 542

Willick, J.A. 1999, ApJ, 516, 47

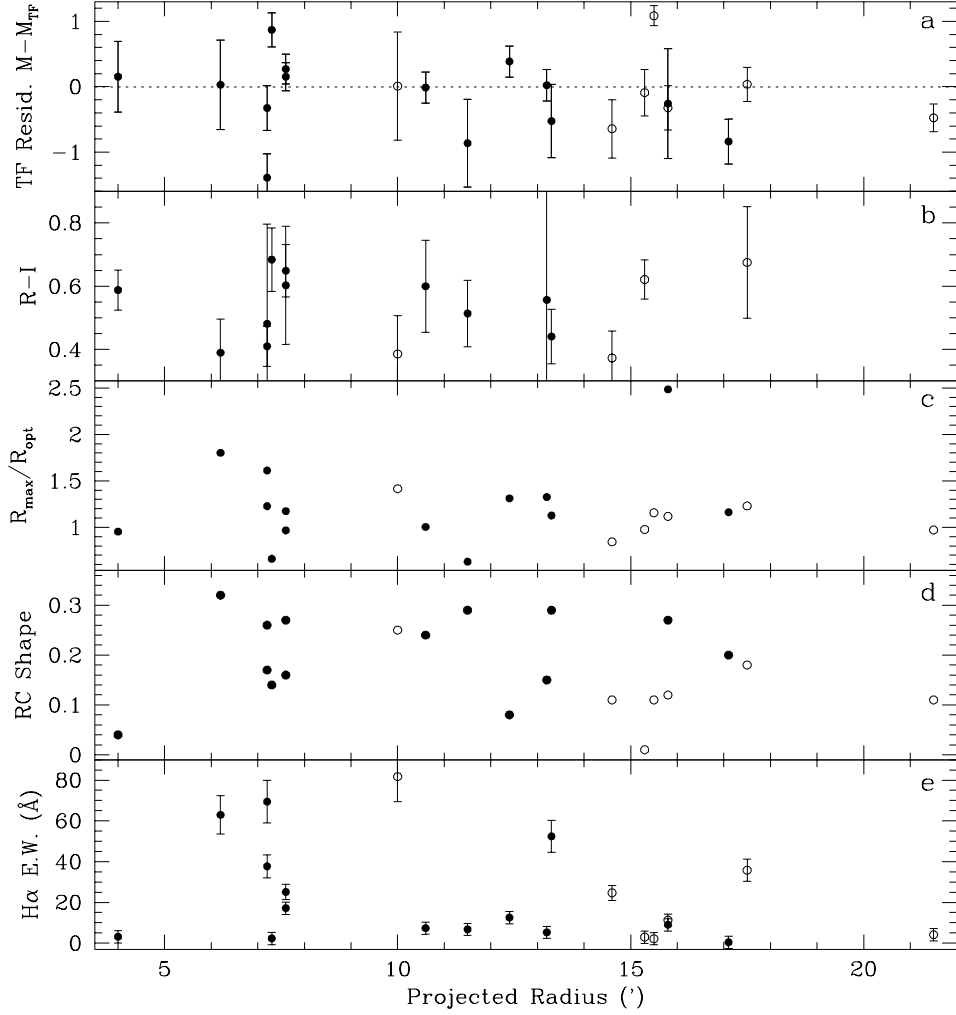


Fig. 5.— Some properties of the emission-line galaxies plotted versus projected distance to the center of the cluster. Filled (open) circles represent cluster (foreground and background) galaxies. Panel (a) shows the residuals of the Tully-Fisher data where the error bars derive from a quadrature sum of the errors in the magnitudes, velocity widths, and the template zero-point. Panels (b) and (c) give the  $R - I$  colors and the extent of the  $H\alpha$  rotation curve (normalized by the optical radius), respectively. Panel (d) displays the outer gradient, or shape, of the rotation curve, and Panel (e) plots the  $H\alpha$  equivalent widths.

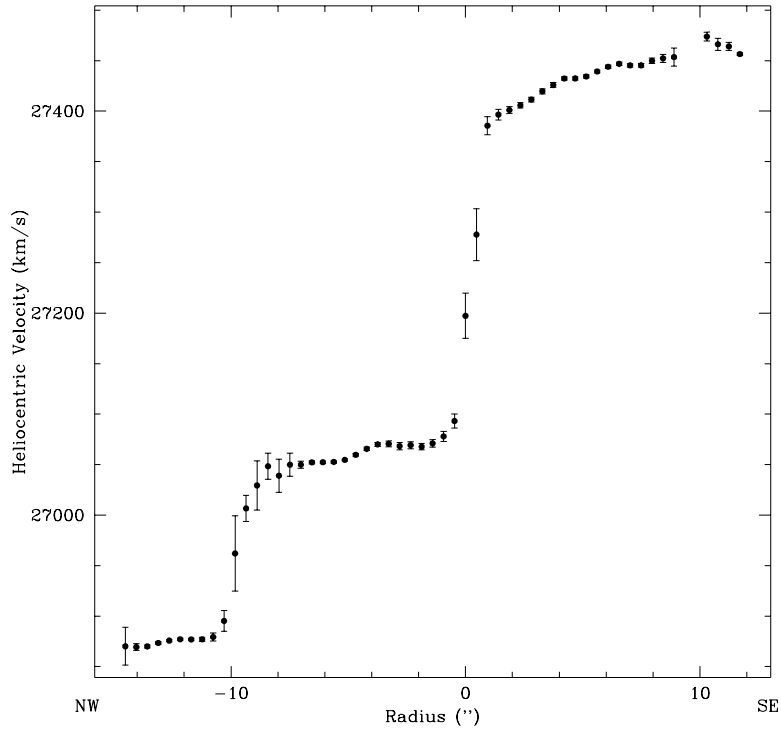


Fig. 6.— The observed rotation curve for AGC 251908 and its tidally-connected companion. No rotation is seen in the companion galaxy due in part to the discrepancy in the position angle of its “disk” and that used for the long-slit spectroscopic observation.

TABLE 1. Target Galaxy Sample

| Names   | R.A.<br>h m s | Dec.<br>d m s | $V_{\odot}$<br>km s <sup>-1</sup> | RC code |
|---------|---------------|---------------|-----------------------------------|---------|
| 251826  | 150719.5      | +055729       | 29630                             | 1       |
| 251827  | 150729.3      | +055446       | 28739                             | 1       |
| 251829  | 150736.8      | +055819       | 21302                             | 1       |
| 251831  | 150743.8      | +055738       | 26064                             | 1       |
| 251907  | 150744.3      | +054736       | 23714                             | 0       |
| 251910  | 150748.5      | +054452       | 24088                             | 0       |
| 251833  | 150748.6      | +055325       | .....                             | 0       |
| 251909  | 150753.9      | +054424       | 28858                             | 1       |
| 251913  | 150801.4      | +054126       | 22019                             | 1       |
| 251835  | 150803.4      | +055919       | .....                             | 0       |
| 251838  | 150810.0      | +055147       | 24820                             | 1       |
| 250190b | 150812.4      | +055452       | 22240                             | 2       |
| 250190  | 150813.7      | +055427       | .....                             | 0       |
| 251843  | 150816.9      | +055442       | 28307                             | 1       |
| 251844  | 150817.7      | +054648       | 21805                             | 1       |
| 251851  | 150820.8      | +060811       | .....                             | 0       |
| 251853  | 150821.5      | +054757       | 10594                             | 2       |
| 251854  | 150821.6      | +054849       | .....                             | 0       |
| 251855  | 150823.4      | +055630       | 22250                             | 0       |
| 251856  | 150824.6      | +055318       | .....                             | 0       |
| 251859  | 150826.7      | +060950       | .....                             | 0       |
| 9752    | 150827.5      | +055559       | 23369                             | 0       |
| 251862  | 150829.1      | +061011       | 23523                             | 1       |
| 250201  | 150830.4      | +055556       | 26670                             | 0       |
| 251863  | 150830.4      | +060024       | .....                             | 0       |
| 250201b | 150831.3      | +055613       | .....                             | 0       |
| 250205  | 150832.1      | +055059       | 25780                             | 2       |
| 251905  | 150832.6      | +055052       | 25680                             | 1       |
| 251869  | 150833.9      | +055656       | 22100                             | 0       |
| 251871  | 150834.4      | +055907       | .....                             | 0       |
| 251873  | 150835.0      | +055232       | 25260                             | 0       |
| 251874  | 150836.3      | +054231       | 10505                             | 1       |
| 251880  | 150841.7      | +060009       | 24000                             | 0       |
| 250216  | 150842.0      | +060115       | 23998                             | 0       |
| 251882  | 150842.8      | +060003       | .....                             | 0       |
| 251883  | 150843.2      | +055032       | 25316                             | 1       |
| 251885  | 150845.8      | +060037       | .....                             | 0       |
| 251886  | 150845.9      | +055005       | .....                             | 0       |
| 251887  | 150846.1      | +055031       | 23965                             | 1       |
| 251888  | 150847.2      | +055305       | 26013                             | 2       |
| 251889  | 150847.9      | +055439       | .....                             | 0       |
| 251891  | 150851.2      | +055557       | 23372                             | 0       |
| 251895  | 150856.7      | +055952       | 24203                             | 1       |
| 251897  | 150900.3      | +055734       | 21391                             | 1       |
| 251906  | 150904.3      | +054506       | 22074                             | 0       |
| 251900  | 150910.2      | +055727       | 10548                             | 1       |
| 251908b | 150913.8      | +055130       | 24177                             | 2       |
| 251908  | 150914.5      | +055121       | 27253                             | 1       |
| 251912  | 150914.7      | +061523       | 15970                             | 1       |
| 251915  | 150918.7      | +060708       | 15849                             | 1       |
| 251911  | 150918.9      | +060703       | 23657                             | 1       |
| 251902  | 150919.2      | +055638       | .....                             | 0       |

TABLE 2. Galaxy Spectroscopic Parameters

| Name   | $T_{\text{exp}}$<br>sec | $V_{\text{cmb}}$<br>km s <sup>-1</sup> | $W_{\text{obs}}$<br>— | $W$<br>km s <sup>-1</sup> | $W_{\text{cor}}$<br>— | $i$<br>° | $\log W_{\text{cor}}$ |
|--------|-------------------------|----------------------------------------|-----------------------|---------------------------|-----------------------|----------|-----------------------|
| (1)    | (2)                     | (3)                                    | (4)                   | (5)                       | (6)                   | (7)      | (8)                   |
| 251826 | 1200                    | 29812(08)                              | 276                   | 253                       | 274                   | 76       | 2.438(032) *          |
| 251827 | 900                     | 28921(09)                              | 291                   | 262                       | 369                   | 47       | 2.567(046) *          |
| 251829 | 2100                    | 21484(12)                              | 199                   | 189                       | 242                   | 55       | 2.384(073)            |
| 251831 | 1200                    | 26246(15)                              | 150                   | 199                       | 225                   | 67       | 2.353(087) *          |
| 251909 | 900                     | 29040(08)                              | 508                   | 468                       | 528                   | 68       | 2.723(019) *          |
| 251913 | 2700                    | 22201(09)                              | 277                   | 257                       | 327                   | 53       | 2.514(044) *          |
| 251838 | 2100                    | 25001(08)                              | 195                   | 175                       | 225                   | 53       | 2.352(047) *          |
| 251843 | 1200                    | 28488(10)                              | 260                   | 234                       | 360                   | 41       | 2.556(070) *          |
| 251844 | 3000                    | 21986(09)                              | 245                   | 233                       | 269                   | 65       | 2.430(030)            |
| 251862 | 3000                    | 23703(09)                              | 352                   | 321                       | 343                   | 79       | 2.535(027)            |
| 251905 | 1500                    | 25861(13)                              | 169                   | 149                       | 177                   | 62       | 2.247(089)            |
| 251874 | 300                     | 10686(08)                              | 179                   | 175                       | 239                   | 47       | 2.378(058) *          |
| 251883 | 2700                    | 25496(10)                              | 479                   | 453                       | 496                   | 73       | 2.696(033)            |
| 251887 | 2100                    | 24145(08)                              | 304                   | 280                       | 326                   | 64       | 2.513(027)            |
| 251895 | 2700                    | 24383(11)                              | 329                   | 316                       | 336                   | 81       | 2.526(039) *          |
| 251897 | 2100                    | 21571(12)                              | 320                   | 299                       | 321                   | 78       | 2.506(025) *          |
| 251900 | 300                     | 10728(10)                              | 148                   | 145                       | 155                   | 78       | 2.192(107) *          |
| 251908 | 1500                    | 27433(09)                              | 401                   | 367                       | 470                   | 53       | 2.672(030) *          |
| 251912 | 600                     | 16149(08)                              | 371                   | 358                       | 382                   | 72       | 2.582(025) *          |
| 251915 | 2100                    | 16028(11)                              | 232                   | 219                       | 293                   | 52       | 2.468(043) *          |
| 251911 | 2100                    | 23836(13)                              | 138                   | 119                       | 144                   | 60       | 2.157(109) *          |



TABLE 3. Galaxy Photometric Parameters

| Names  | T   | $\theta$<br>' | PA<br>° | $\epsilon$ | $R_d$<br>" | $R_{opt}$<br>" | $m_I$ | $M_I$      | $R - I$ |
|--------|-----|---------------|---------|------------|------------|----------------|-------|------------|---------|
| (1)    | (2) | (3)           | (4)     | (5)        | (6)        | (7)            | (8)   | (9)        | (10)    |
| 251826 | 5   | 18            | 90      | 0.724(014) | 2.5        | 7.2            | 16.98 | -20.39(09) | 0.67 *  |
| 251827 | 5   | 15            | 34      | 0.314(036) | 3.0        | 7.7            | 15.79 | -21.51(03) | 0.62 *  |
| 251829 | 5:  | 13            | 154     | 0.417(050) | 1.1        | 4.2            | 16.33 | -20.54(05) | 0.44    |
| 251831 | 5   | 12            | 84      | 0.595(017) | 1.7        | 5.9            | 16.23 | -20.64(06) | 0.51 *  |
| 251909 | 5   | 15            | 110     | 0.613(028) | 1.6        | 5.3            | 15.79 | -21.53(04) | — *     |
| 251913 | 3   | 17            | 135     | 0.380(041) | 2.3        | 8.9            | 15.02 | -21.75(04) | — *     |
| 251838 | 5:  | 7             | 63      | 0.394(022) | 2.0        | 6.4            | 15.71 | -21.16(03) | 0.41 *  |
| 251843 | 6   | 4             | 67      | 0.241(042) | 2.0        | 6.9            | 16.09 | -21.18(03) | 0.59 *  |
| 251844 | 5   | 11            | 137     | 0.563(037) | 1.5        | 5.6            | 16.49 | -20.38(06) | 0.60    |
| 251862 | 1   | 13            | 115     | 0.727(019) | 3.4        | 10.6           | 15.72 | -20.83(11) | 0.56    |
| 251905 | 6   | 6             | 125     | 0.524(023) | 0.8        | 2.8            | 17.94 | -18.93(04) | 0.39    |
| 251874 | 4   | 15            | 173     | 0.317(031) | 6.2        | 17.8           | 14.54 | -20.61(04) | 0.37 *  |
| 251883 | 4   | 7             | 47      | 0.687(046) | 2.6        | 8.5            | 15.33 | -21.54(06) | 0.68    |
| 251887 | 5   | 8             | 8       | 0.553(037) | 1.7        | 6.0            | 16.02 | -20.85(04) | 0.65    |
| 251895 | 7   | 7             | 150     | 0.800(053) | 1.7        | 7.2            | 15.44 | -21.43(16) | 0.48 *  |
| 251897 | 6   | 8             | 86      | 0.752(032) | 1.9        | 7.2            | 16.19 | -20.68(11) | 0.60 *  |
| 251900 | 5   | 10            | 6       | 0.756(021) | 2.2        | 7.6            | 16.62 | -18.53(06) | 0.39 *  |
| 251908 | 5   | 12            | 137     | 0.395(038) | 2.0        | 7.8            | 15.35 | -21.84(03) | — *     |
| 251912 | 0   | 21            | 45      | 0.642(019) | 4.4        | 12.6           | 14.03 | -21.69(09) | — *     |
| 251915 | 5:  | 16            | 110     | 0.372(021) | 2.4        | 8.8            | 15.04 | -20.98(04) | — *     |
| 251911 | 7:  | 16            | 110     | 0.489(110) | 0.8        | 3.2            | 18.34 | -18.53(08) | — *     |